Microfluidics and Nanofluidics (2020) 24:36
https://doi.org/10.1007/s10404-020-02343-5

RESEARCH PAPER

Self-powered microfluidic pump using evaporation from diatom biosilica thin films

Hunter Jarrett[1] · Micah Wade[1] · Joseph Kraai[2] · Gregory L. Rorrer[2] · Alan X. Wang[3] · Hua Tan[1]

Received: 23 November 2019 / Accepted: 11 April 2020

Abstract

In recent years, researchers have successfully applied diatom biosilica to molecular detection platforms including Surface-Enhanced Raman Scattering (SERS) optofluidic sensors that are currently capable of detecting a variety of biological and chemical molecules at concentrations as low as 10^{-10} M. This study investigates the feasibility of an SERS device that couples the sensing and pumping capabilities of diatom biosilica thin films by determining flow rate limitations and stability. In this paper, we quantify the ability of porous diatom biosilica thin films to continuously pump deionized (DI) water from a reservoir via wicking flow by utilizing the strong capillary forces of the porous film coupled with evaporation. Our microfluidic device is comprised of a narrow horizontal reservoir fixed to a horizontal capillary whose end contacts a diatom biosilica film. Flow rates were controlled by altering the size and/or temperature of the biosilica porous film, determined by tracking the liquid meniscus displacement in the reservoir, and correlated with a modified laminar boundary-layer model. System stability was observed by tracking flow rates over the course of a given experiment, image analysis of the meniscus contacting the film, and a flow duration study. We found that for untreated DI water bubbles begin to form in the capillary tube at temperatures above 40 °C, but degassed water remains stable at temperatures of 90 °C and below. The pumping capabilities of the films ranged from 0.11 to 10.46 µL/min, matched theoretical predictions, demonstrated stable flow trends, and maintained flow for over 48 h.

Keywords Microfluidic pump · Biosilica · Surface-enhanced Raman scattering (SERS) · Evaporation · Thin films

1 Introduction

Interest in microfluidic lab on chip (LOC) research has grown significantly over the past decades because of its ability to reduce cost, sample size, and process time (Boyd-Moss et al. 2016; Convery and Gadegaard 2019; Ohno et al. 2008; Sackmann et al. 2014; Turner 2013). Microfluidic LOC devices enable process intensification by utilizing some unique characteristics of microscopic flows such as large surface-to-volume ratio, laminar flow, surface tension, and short diffusion distance (Squires and Quake 2005). In modern times, microfluidic technology is widely used in chemical, biological, and medical applications (Convery and Gadegaard 2019; Laser 2004; Ohno et al. 2008; Sackmann et al. 2014; Xiao-Ming et al. 2019).

As a key component of microfluidic systems, pumps need to accurately transport fluid throughout a system for successful operation (Laser 2004). Various microfluidic pumping methods have been developed for specific operations and can be classified into two categories: active micro-pumps and passive micro-pumps (Laser 2004). Active micro-pumps use an external power source to drive fluid flow, while passive micro-pumps achieve fluid flow using inherent properties of the fluid and geometric system design, with no requirement for an external power source. Active micro-pumps can be further broken down into mechanical pumps, which generate flow through the oscillation or rotation of a mechanical device, and non-mechanical pumps, which use electro- and magneto-kinetic, acoustic, chemical, or bubble-driven pumping techniques to induce flow (Laser 2004). Mechanical

✉ Hua Tan
hua.tan@wsu.edu

[1] School of Engineering and Computer Science, Washington State University-Vancouver, Vancouver, WA 98686, USA

[2] School of Chemical, Biological and Environmental Engineering, Oregon State University, Corvallis, OR 97331, USA

[3] School of Electrical Engineering and Computer Science, Oregon State University, Corvallis, OR 97331, USA

Published online: 22 April 2020

micro-pumps offer a large range of control and can supply a flow indefinitely, but are complex, expensive, produce high pressures, can damage living cells, and have large fluid dead volumes (Chen et al. 2012; Goedecke et al. 2002; Woias 2005). A specific example of an active mechanical pump that is widely used for institutional research is a syringe-based pump that operates using a lead screw to depress a plunger at a specific rate (Li et al. 2019). However, these systems still require improvement, because once a syringe is completely depressed, liquid remains trapped in the capillary network leading to the microfluidic device. Active non-mechanical micro-pumps are capable of accurately supplying small amounts of fluid indefinitely without the large fluid dead volumes present in mechanical micro-pumps, but still rely on external signals to initiate and cease pumping, which increases their cost and complexity making them undesirable for point-of-care diagnostics. Passive pumping devices primarily use capillary action coupled with geometric relations of the piping system to control flow rate. Researchers have utilized passive flow techniques to develop a wide range of devices capable of performing different tasks. For example, filter paper has been widely used to provide a capillary pressure, drawing fluid throughout a microfluidic system (Wang et al. 2010). The main limitation in capillary networks is that once the entire system is filled with liquid, no more fluid can be pumped and flow ceases. Interestingly, passive components have been utilized in active mechanical pumps to increase pump simplicity and reliability by incorporating diffuser/nozzle systems instead of valves to control flow from an inlet to an outlet (Xu et al. 2019).

To realize continuous flow in micro- and nano-scale systems, various capillary pumping platforms have been proposed to couple capillary action with evaporation from mediums such as open capillaries, gels, and porous media, similar to the microfluidic networks plants use to transport fluid. Imitation of plants has played an important role in microfluidic device development, as researchers have tried to mimic and modify natural systems to accomplish specific tasks (Chen et al. 2012; Jingmin et al. 2012; Kim et al. 2016). Table 1 provides a summary of previous studies on active and passive capillary-evaporation (CE) pumps including experimental data on flowrates, evaporation mediums, and pumping durations. In a completely passive CE-based pump, flow rates are affected by the ambient temperature, humidity, and airflow speed in addition to the exposed surface area of the evaporating liquid. By adding active methods to CE pumps, such as a heating element, a fan to increase flow rate over the exposed liquid surface area, or pumping in strictly controlled environments, users gain a wider range of control over the flow rate but make the system more complicated. Active CE pumps are still subject to ambient conditions, but precise flow rates can be achieved through feedback loops coupled with algorithms to vary substrate temperature and airflow speed. A CE pump application that has garnered interest recently is a sweat sensor that uses body heat to increase flow rate (Nie et al. 2015). The concept was then improved and incorporated into real-time sweat rate monitoring device with an electrochemical sensor (Xiao-Ming et al. 2019).

Table 1 Summary of studies investigating the combination of capillarity and evaporation to achieve continuous flow

Previous CE studies	Active pumping method	Flowrate (μL/h)	Evaporation medium	Operating time (U = unreported)
Juncker et al. (2002)	Airflow	72	Open channel	U
Effenhauser et al. (2002)	None	0.6–60	Adsorption agent	Days
Goedecke et al. (2002)	Airflow	25	Open channel	U
Namasivayam (2003)	Airflow/Heat	0.3	Open channel	2 h
Zimmermann et al. (2005, 2007)	Heating	4.3	Open channel	U
Guan et al. (2006)	None	181	Open channel	Several Hours
Xu et al. (2008)	None	32.4-140	Paper medium	400 h
Choi et al. (2009)	None	0.008-0.32	Porous gel	6 h
Lynn and Dandy (2009)	None	2.1	Open reservoir	75 min
Chen et al. (2012)	Heater	800	Porous filter	U
Jingmin et al. (2012)	Heater	67.2	Porous gel	U
Zhang et al. (2014)	Piezoelectric	84.6	Paper medium	U
Temiz et al. (2014)	Heater	28.8	Open channel	U
Nie et al. (2015)	None	0.44–7.2	Porous structure	U
Kim et al. (2016)	Heater	30	Porous hydrogel	Days
Xiao-Ming et al. (2019)	None	14.1	Porous structure	U

Our study investigates using a diatom biosilica thin film with porous micro- and nano- structures to drive continuous flow in a microfluidic device utilizing CE pumping methods. Diatoms are naturally occurring single-celled microalgae that biomineralize silica shells, called frustules, patterned with hierarchal micro- to nano-scale periodic pore arrays (Ever Aguirre et al. 2018; Jeffryes et al. 2011; Kong et al. 2017; Zhou and Kim 2016). There is significant interest in integrating diatoms and their biosilica frustules into devices such as chemical/biological sensors, solar batteries, electroluminescent devices, drug delivery systems, microfluidic transport systems, and grown 3D nano-computers (Gordon et al. 2009; Jeffryes et al. 2011; Kong et al. 2017; Marshall et al. 2012). The application of most relevance to this study is chemical/biological detection using surface-enhanced Raman scattering (SERS), where the diatom frustules are functionalized with silver nanoparticles (Ag NP) (Kearns et al. 2016; Kitahama and Ozaki 2016; Lin et al. 2013; Ren et al. 2013; Taylor et al. 2016). Photonic crystal structures of diatom biosilica provide novel capabilities for the control and manipulation of light for chemical/biological detection using the SERS technique. Raman spectra act as unique molecular fingerprints that allow for the identification of specific molecular species, but they are plagued by low sensitivity (Zhou and Kim 2016). Surfaces are 'enhanced' by treating the surface with noble metal nanostructures, which amplify signals through localized surface plasmon resonance-induced electromagnetic field enhancement (Long 2002; Otto 1992; Taylor et al. 2016). SERS device enhancement factors typically range from 10^6–10^9 (Kong et al. 2017; Zhou and Kim 2016) and can achieve single molecule-level detection (Kong et al. 2016; Taylor et al. 2016). Microfluidic approaches for SERS technology have traditionally been performed in lab using fabricated PDMS or capillary microfluidic channels treated with noble metals, but can be complicated when trying to create uniform hotspot density and when attempting to generate mixing flows to increase detection (Zhou and Kim 2016). Diatom frustule's hierarchical nano-scale photonic crystal features can enhance local optical fields inside and on the surface of diatoms, which in turn can enhance localized surface plasmon resonance of self-assembled metal nanoparticles (Kong et al. 2017). The nature of the diatom frustule allows for integration of the Ag NPs inside of the frustule nano-pores, providing high density hot spots and strongly coupled optical resonances with the photonic crystal structure of the diatom frustules (Kong et al. 2016; Sivashanmugan et al. 2019).

The ultimate goal of this research is to combine the SERS detection properties with the CE pumping capability of diatom frustules for rapid, ultra-sensitive detection of chemical and biological molecules. The super hydrophilic nature of the diatom biosilica material coupled with evaporation is capable of concentrating analyte molecules on the SERS substrate. Our previous research has already demonstrated the sensing capability of diatom biosilica-based microfluidics (Kong et al. 2016; Sivashanmugan et al. 2019), but these devices are complicated and require several steps to initiate flow for detection. This presents numerous hurdles in an attempt to automate the detection processes, limiting applicability. Using the CE pumping characteristics in conjunction with SERS sensing, diatom biosilica-based microfluidics can automatically fill themselves and generate a self-sustained passive flow from the reservoir through a microfluidic channel to the sensing region. Unlike those reported evaporation-driven microfluidics listed in Table 1, the pumping and sensing functions in our proposed devices are accomplished with one component (i.e., diatom porous film), which reduces the size, complexity, and cost of the sensor, maintains the capillary pressure to drive target molecules through the sensor area, and improves the robustness and portability. Additionally, compared to the other types of porous media used in CE pumps, the diatom biosilica material is highly porous (porosity > 0.95) and super-hydrophilic, which means that such material has significantly large surface-to-volume ratio and strong capillary force. As we have already proved the sensing capability of the diatom-based SERS substrate from our previous research, the focus of this study is to explore the pumping capability of diatom biosilica porous films as well as the factors affecting the pumping and the stability of the system.

Specifically, this study creates an active CE pump that uses a thin porous film of *Pinnularia* sp. biosilica fixed to a glass substrate as the capillary pump that drives the fluid from a reservoir into the film and represents the first phase of development. The active component is a silicon heater fixed to the bottom of a microscope holder with a conductive adhesive and controlled with a feedback loop that maintains a constant film temperature. Biosilica films with different areas at varied substrate temperatures are used to study system stability. Evaporation coupled with the capillary action creates a steady-state flow from the reservoir into the biosilica film. The flow rate is determined by repeatedly imaging the liquid meniscus in the reservoir over the course of the experiment, finding the linear displacement of the meniscus in the reservoir from image to image, using the known reservoir diameter, and utilizing the image time stamp to calculate the elapsed time between images. Meniscus displacement is determined using an in-house developed MATLAB image processing code. Ultimately, flow rate trends for different film areas and substrate temperatures are obtained to highlight their impacts on system stability. An untreated and degassed DI water analysis is performed to understand degassing's impact on system stability and flow rate. The degassed liquid flow trends are compared to theoretical models to determine whether the system trends as expected.

2 Experimental method

In this section, we describe the proposed microfluidic pump, the methods of data collection, and the techniques used to process the data. The pump's characterization and fabrication are provided in Sect. 2.1. The apparatus used to secure the pump and record data will be presented in Sect. 2.2. Finally, Sect. 2.3 will explain the experimental procedures used to initiate flow and the software used to gather/analyze the data.

2.1 Microfluidic pump

The microfluidic pump consists of a long and narrow horizontal reservoir that is connected to a biosilica thin film with a horizontal capillary tube, as illustrated in Fig. 1. The reservoir is a 1 mL Fisherbrand™ Kolmer Serological Pipette with a 2.71 mm inner diameter (ID). The polyetheretherketone (PEEK) capillary tube, with an ID of 150 µm and 5 cm length, was fixed to the center of the pipette using a waterproof silicone adhesive and a leveling table to maintain a horizontal profile during the drying process. Finally, the biosilica film fixed to a microscope slide was placed at end of the capillary using a custom x, y, and z linear axis system. Maintaining a horizontal profile minimizes the impact of gravity on the system and allows the hydrophilic properties of the film to control flow from the reservoir.

2.1.1 Biosilica film fabrication

Multi-layered *Pinnularia* sp. diatom biosilica thin films were created using a drop-cast film fabrication method on microscope slides, as shown in Fig. 2. To eliminate organic contaminants, slides were cleaned in an ultrasonic bath filled with 1% Liquinox detergent solution, rinsed with water and ethanol, and then treated with a UV-Ozone cleaner at 120 °C for 24 h. The slides were covered with parafilm as shown in Fig. 2a, and square patterns were cut from the film using a stencil and utility knife as shown in Fig. 2b. The stencil was created in SketchUp, printed to scale, and checked with calipers. The diatom biosilica frustules were homogeneously suspended in water before being uniformly pipetted inside the square pattern on the microscope slide as shown in Fig. 2c, and held at a temperature of 35 °C to decrease surface tension and increase evaporation rate. Figure 3a shows the experimental image of liquid diatom suspension dispensed on the exposed section of microscope slide. Upon complete water evaporation, a biosilica thin film, approximately 25 µm thick, was left on the exposed portion of substrate and the parafilm was then removed, as illustrated in Fig. 2d. Figure 3b shows the dried diatom biosilica film before parafilm is removed. To fix the biosilica film to the substrate surface, the substrates were heat treated in a UV-Ozone cleaner at 120 °C for 12 h to oxidize residual organic contaminants. Square films of 9, 16, 25, 36, 49, 64, and 81 mm^2 were fabricated in our study. Larger film sizes were attempted, but a disparity in film homogeneity was noted for films above 81 mm^2, as demonstrated in Fig. 3c. The microstructure of the fabricated biosilica film of 81 mm^2 was imaged with a scanning electron microscope (SEM), as shown in Fig. 4a, which clearly demonstrates a highly porous structure. A close-up of the single diatom frustule from our previous publication (Kraai et al. 2019) is provided in Fig. 4b.

2.2 Apparatus design

An optical apparatus was designed to hold the microfluidic assembly, while allowing visualization of the meniscus in the pipette or the meniscus protruding from the capillary tip into the biosilica film. The apparatus consisted of a custom base, camera clamp, microscope light holder, microscope stage, x, y, and z linear slide rails, and a pipette holder, with the CAD model illustrated in Fig. 5a and the experimental system pictured in Fig. 5b.

Images of the receding meniscus in the pipette and the meniscus contacting the biosilica film were taken with a Thorlabs 1545 M scientific camera attached to a 6.5 × Navitar microscope lens. Ambient temperature and humidity were captured with a DHT 22 sensor (± 0.5 °C and 2–5%) and a hygrometer thermometer clock (± 1 °C and ± 5%). The DHT 22 sensor and the hygrometer thermometer clock were calibrated using a Kestrel 3000 handheld weather meter (± 0.1 °C and ± 0.1%). An OMEGA (SRMU100101) silicon heating element was controlled using feedback from an

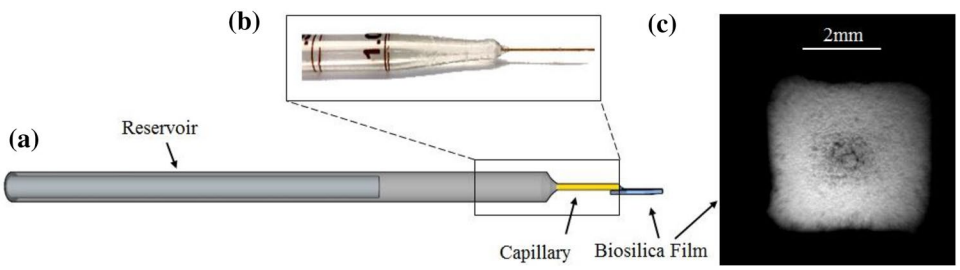

Fig. 1 Microfluidic pump overview: **a** schematic, **b** pipette and capillary tube used in experiment (zoom-in), and **c** diatom biosilica porous thin film

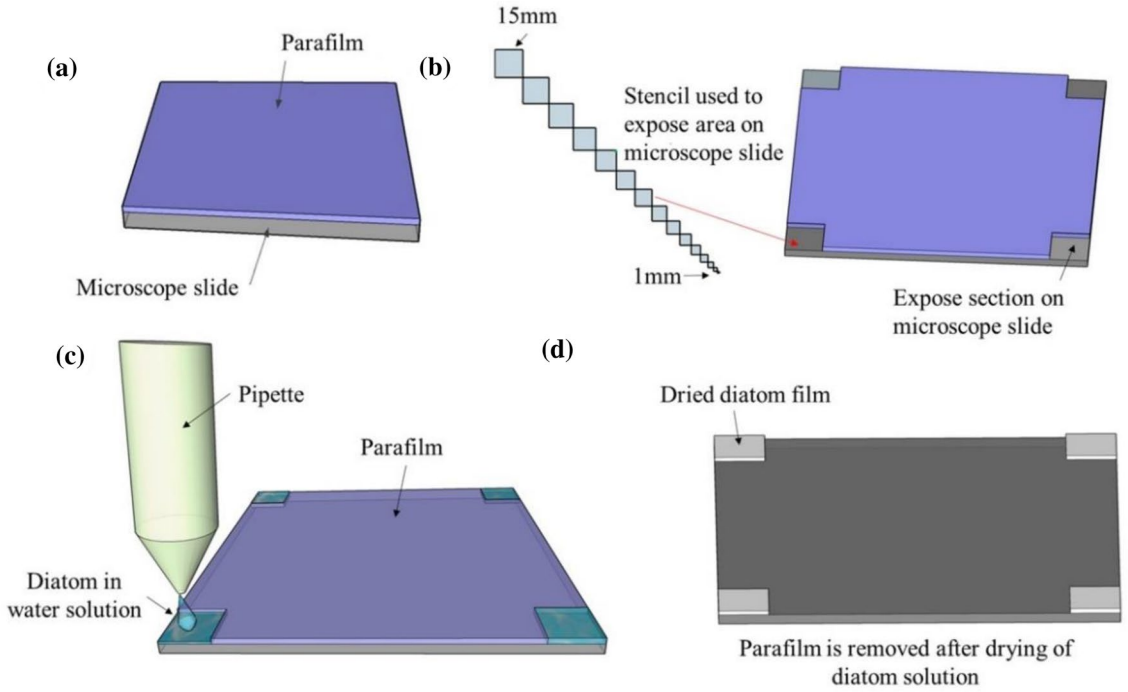

Fig. 2 The film fabrication process: **a** the microscope slide is covered with parafilm, **b** a stencil is used to remove section of the parafilm at the corners, exposing a specific area on the microscope slide, **c** liquid water with suspended diatom biosilica is pipetted onto the exposed area of the microscope slide, and **d** the liquid water evaporates leaving a dried biosilica film in the exposed area of the microscope slide and then parafilm is removed

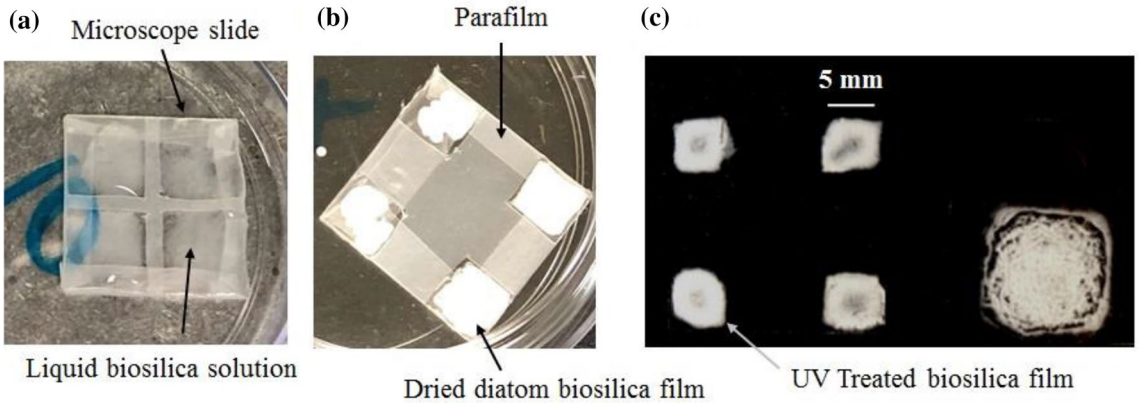

Fig. 3 Experimental images of the film fabrication process: **a** drop-cast liquid diatom suspension on exposed surface of microscope slide, **b** dried biosilica film before parafilm is removed, and **c** dried film with parafilm removed and example of the disparity of the homogeneity between smaller and larger surface area films

Adafruit 10 K Precision Epoxy Thermistor-3950 connected to an Arduino Mega 2560, and a solid-state relay to regulate substrate temperature.

2.3 Experimental procedures

In our experiments, the reservoir was either filled with untreated or degassed DI water (which was degassed by boiling). To initiate flow, a pipette bulb was used to apply pressure at the open end of the pipette, causing liquid to bulge from the capillary tip and contact the biosilica film. The bulb was removed and liquid spread throughout the film, causing the dry, white, opaque silica to become wetted and semi-translucent. As evaporation occurs in the diatom film, the meniscus in the pipette reservoir recedes due to mass conservation. After flow was initiated, the

meniscus contacting the film was observed and the transition from an opaque film to a translucent film was noted. Once the film was translucent and the meniscus position stopped fluctuating from the flow initiation, the time was noted, and the system was checked at the beginning and end of each day. If the reservoir emptied before the next system check, the previous time was reported as the flow duration.

Flow experiments ranged anywhere from a few hours to a few days depending on the size and temperature of the substrate and whether flow duration or rate was being determined. To measure the flow rate, several high-contrast images of the receding meniscus in the horizontal pipette were taken over varied time intervals using a camera, as shown in Fig. 6b, c. The meniscus location was found in each photo using in-house developed MATLAB image

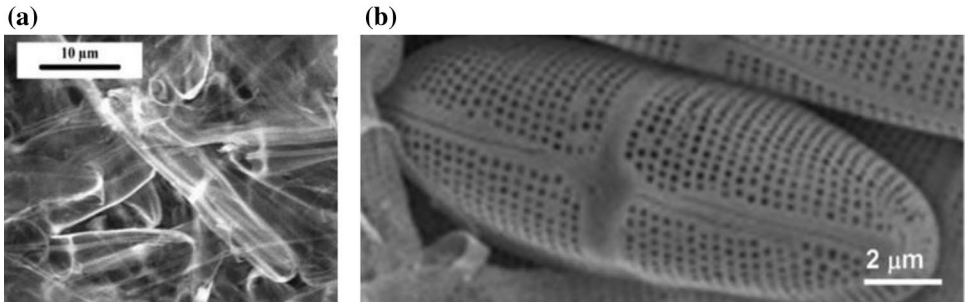

Fig. 4 *Pinnularia* sp biosilica film stacking and shape: **a** biosilica film stacking taken with a scanning electron microscope (SEM), **b** single *Pinnularia* sp. frustule (Kraai et al. 2019)

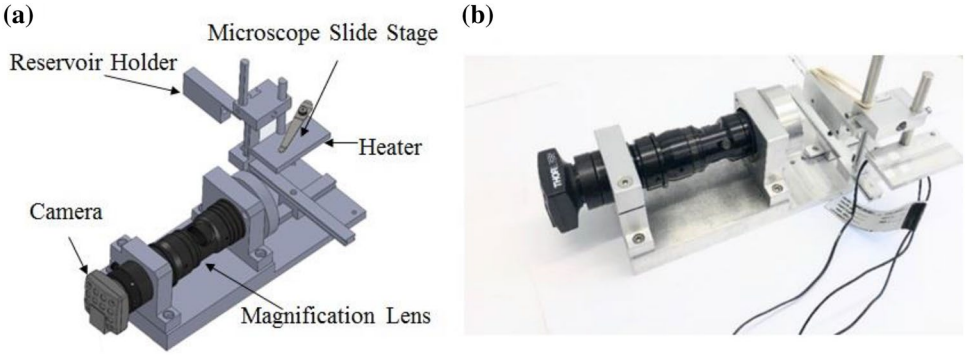

Fig. 5 System overview: **a** CAD model of system components and **b** actual experimental setup

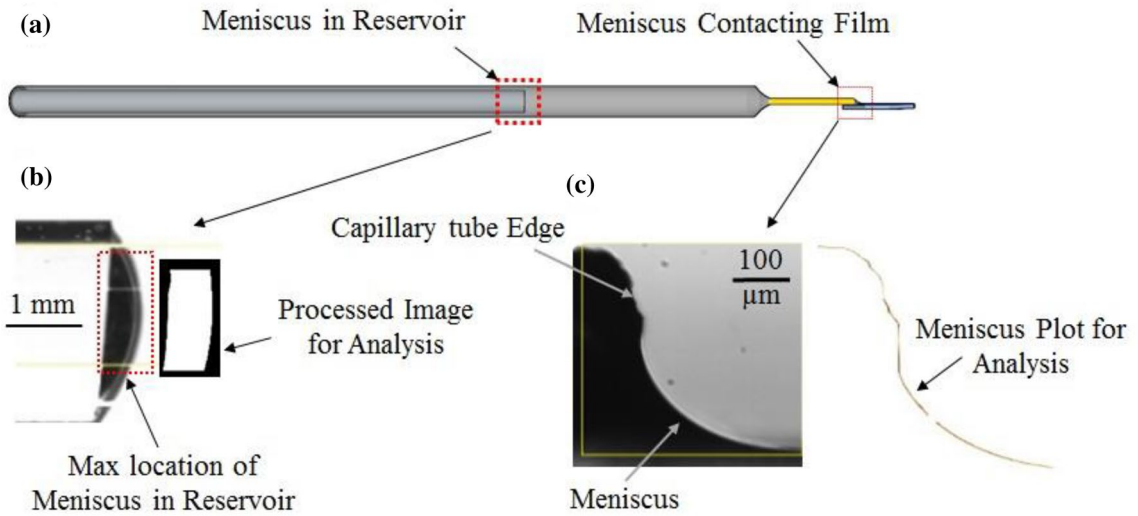

Fig. 6 Areas of interest for data collection and image processing: **a** microfluidic pump with key areas marked, **b** meniscus in pipette ajoined with processed image of mensicus in pipette using MATLAB, and **c** biosilica film meniscus and processed meniscus profile using MATLAB

processing code. A 1 mm microscopic slide scale was used to translate pixel displacement to millimeter displacement between photos and converted to volumetric displacement. Photos were time stamped and the difference between the time stamps of each consecutive photo were used to calculate flow rate. To determine whether the evaporation from the open end of the reservoir impacts flow rate, a flow rate analysis was performed separately when the capillary was not connected to the biosilica film. To check the stability of the system during the operation, the meniscus outside the capillary tip contacting the diatom film was constantly monitored, as shown in Fig. 6c. The meniscus locations obtained from experimental images were then overlaid with one another to check for instabilities, or fluctuations in meniscus location. When an unstable flow pattern was observed, further analysis was performed to remedy the underlying cause.

3 Theoretical analysis

There are three primary theories that provide the basis for predicting how the microfluidic pump will behave: pipe flow (Sect. 3.1), capillary pressure provided by a porous microstructure (Sect. 3.2), and mass transfer via evaporation (Sect. 3.3). The maximum flow through the capillary tube is determined by the pressure provided by the porous diatom thin film. Once the film becomes completely wetted, flow will be determined by the evaporation rate. If the evaporation rate exceeds the maximum possible flow rate through the capillary, the film will no longer pump liquid and the water will recede into the capillary tube. The shape of the meniscus protruding from the capillary, as shown in Fig. 7, was studied to understand the stability of the flow during the operation of the microfluidic system. The experimental shape of the meniscus was compared against the numerical simulation using the Surface Evolver-Fluid Interface Tool (SE-FIT®) (SE-FIT 2018) and discussed in Sect. 3.4. A simplified illustration of the flow in system is provided in Fig. 7.

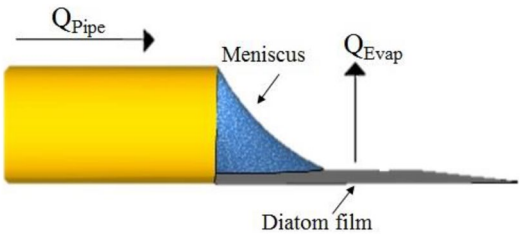

Fig. 7 Illustration of liquid flowing through the capillary tube into the biosilica film and evaporating

3.1 Pipe flow

Pipe flow can approximate flow in the capillary tube and explain why the changing length of the liquid column in the reservoir is negligible through a dimensional analysis. For the laminar flow in a circular pipe, the flow rate can be expressed as $Q_{\text{pipe}} = \pi D^4 \Delta p/(128\ \mu L)$ (White 1991), where Q_{Pipe} is the flow rate, Δp is the pressure difference across the length of the pipe, D is the pipe diameter, μ is the dynamic viscosity, and L is the pipe length. The maximum flow resistance due to the reservoir occurs when the experiment begins. By performing the dimensional analysis $Q \propto D^4 \Delta p/L$, it is clear that the flow in the capillary tube is several orders of magnitude lower than the reservoir, so the transient impact of the decreasing wetted portion of the reservoir during operation can be neglected.

3.2 Capillary pressure from porous thin film

The pressure difference that corresponds to the maximum flow rate possible through the capillary is directly related to the pressure induced by the porous biosilica thin film. The maximum flow rates of the system is capable of producing are due to a dry film, because, once the film is fully wetted, the wicking action of the diatom only pumps liquid lost due to evaporation. If the evaporation rate ever exceeds the maximum possible flow rate through the capillary, flow will not be sustained, and the meniscus will recede into the capillary as the film dries.

The capillary pressure p_c that drives flow in our system is provided by the porous thin film and can be estimated using $p_c = 2\gamma\cos(\theta)/R_c$, where γ is surface tension, θ is contact angle, and R_c is an equivalent capillary radius (Masoodi et al. 2012). The assumed contact angle θ is 0 for the super-hydrophilic film. R_c of the porous diatom layer can be estimated by $R_c = 2A_{\text{int,s}}\varepsilon/(C_{\text{int,s}}(1-\varepsilon))$, where $A_{\text{int,s}}$ is the cross-sectional area of a solid particle, $C_{\text{int,s}}$ is the perimeter of the solid particle, and ε is the porosity of the porous medium (Masoodi et al. 2012). A porosity ε of 96% (Kraai et al. 2019) and a cross-sectional diameter of 11.9 µm (Kraai et al. 2019) were used to determine a capillary radius of 1.43×10^{-4} m. Surface tensions of 0.072 N/m at 25 °C and 0.061 N/m at 90 °C were used to determine a maximum and minimum flow rate for a dry film of 18.1 µL/min and 15.3 µL/min, respectively. Note that evaporation rate should increase at higher temperatures, but the maximum possible flow rates decrease as temperature increases due to a decreasing surface tension. Because diatom frustules are largely hollow, the maximum and minimum flow rates are conservative estimates based on solid particles.

3.3 Prediction of evaporation rate

A standard convective laminar boundary-layer model, as shown in Fig. 8a, with a modified characteristic length is used to estimate the evaporation rate (Bergman and Incropera 2011). The evaporation through the porous thin layer is modeled as a thin liquid film as the diatom layer is highly porous. A recent study on the evaporation from disks shows that boundary layers originate at each edge of a shape and converge in the center during the evaporation (Dollet and Boulogne 2017). Thus, this idea was incorporated into the laminar boundary-layer model by halving the characteristic length, as shown in Fig. 8b.

The hydrodynamic solution can be achieved using the well-known Blasius method (Bergman and Incropera 2011). Velocities are defined through a stream function to satisfy continuity, while new dependent and independent variables are introduced to reduce the momentum equation from a partial differential equation to an ordinary differential equation and solved via a similarity solution assuming a constant geometric relationship, leading to the well-known solution $\delta = 5L/(\mathrm{Re}_L)^{1/2}$, where δ is the boundary-layer thickness, L is the plate length, and Re is the Reynold's number. For our system, the velocity is always defined as $V_\infty = \mu/(\rho L)$, where ρ is density and μ is the dynamic viscosity (White 1991). The species solution is obtained by incorporating the hydrodynamic solution and applying boundary conditions, where the surface of the liquid is 100% saturated and the ambient concentration is subject to the humidity ratio (Dollet and Boulogne 2017). Non-dimensionalisation leads to similarity parameters including the Reynold's (Re) and Schmidt (Sc) numbers ($\mathrm{Sc} = \nu/D_{\mathrm{AB}}$, where ν is kinematic viscosity and D_{AB} is the diffusivity of water vapor into air), which are used to find the mass transfer coefficient for a specific geometry, fluid, and length through the averaged Sherwood ($\overline{\mathrm{Sh}}$) number. For a flat, horizontal plate experiencing laminar flow convective mass transfer, the averaged Sherwood number can be estimated by $\overline{\mathrm{Sh}} = 0.664\mathrm{Re}^{1/2}\mathrm{Sc}^{1/3} = \bar{k}_c L/D_{\mathrm{AB}}$, where $\bar{k}_c$ is the mass transfer coefficient. Once the mass transfer coefficient is determined, the evaporation rate Q_{Evap} can be estimated by (Bergman and Incropera 2011):

$$Q_{\mathrm{Evap}} = \bar{k}_c A_s \frac{M}{R_u}\left(\frac{P_s}{T_s} - H\frac{P_\infty}{T_\infty}\right), \tag{1}$$

where M is the molar mass of water, A_s is the surface area, R_u is the universal gas constant, P_s and P_∞ are the saturated pressure and ambient pressure, respectively, T_s and T_∞ are the saturated temperature and ambient temperature respectively, and H is the relative humidity.

3.4 Meniscus shape

The pressure difference across the meniscus interface formed outside the end of capillary tube above the diatom biosilica film is determine by Young–Laplace equation $\Delta p = \gamma(1/R_1 + 1/R_2)$, where R_1 and R_2 are the principal radii of curvature of the meniscus interface (Kirby 2010). Because the pressure at the interface is directly related to the shape of the meniscus, different flow rates through the capillary tube must experience different meniscus radii. If the shape of the meniscus contacting the diatom is changing, the flow is accelerating or decelerating, i.e., the system has not yet reached the steady state. Therefore, in our study, the meniscus profile is monitored to ensure that the measurements of the flow rate are done when the system is fully stable.

An open-source software SE-FIT (2018) is used to compute the meniscus shape to understand the equilibrium profile of the meniscus during steady-state operation. The tool computes the profile of the liquid–gas interface controlled

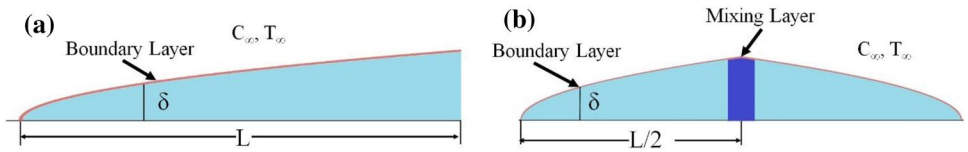

Fig. 8 Boundary-layer illustrations: **a** standard laminar boundary layer and **b** laminar boundary layer under natural convection

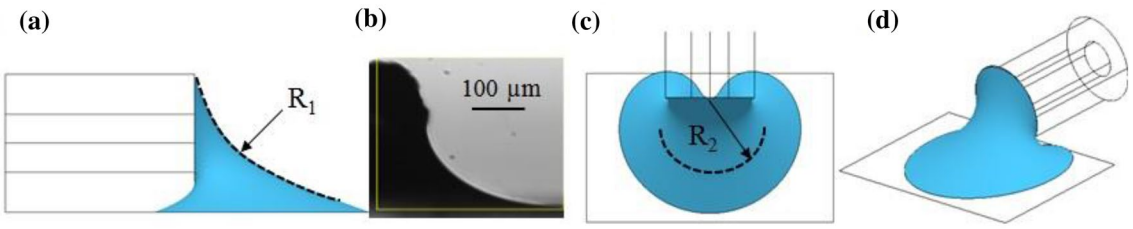

Fig. 9 Simulation of the steady meniscus shape outside the end of the capillary tube over the diatom film: **a** simulated side view, **b** experimental side view, **c** simulated top view, and **d** simulated isometric view

by surface tension and other energies, and subject to various constraints. When performing the SE-FIT simulation, we assume that the only forces dictating the shape of the meniscus are the outer edge of the pipette and the biosilica film, and the meniscus is in contact with the wetted diatom film. Figure 9 plots the predicted meniscus shape at different view angles. The predicted meniscus profile is in good agreement with experiment, as shown in Fig. 9a, b. It is clear that the meniscus shape is a complex surface with two principal curvature radii plotted in Fig. 9a, c. Upon observation of the simulated results, it is also apparent that the shape of R_1 and R_2 changes depending on which portion of the meniscus is being studied.

4 Results and discussion

4.1 Flow duration test

The purpose of the flow duration experiment is to ensure that the pump maintains steady-state conditions over a long period of time. Flow duration is measured at a room temperature of 23 °C and a humidity that fluctuated between 35 and 45%. As stated in Sect. 2.4, to initiate flow, a pressure surge is applied to the open end of the reservoir to cause the liquid to bulge from the capillary tip and contact the diatom film, as shown in Fig. 10. Because of the fluid momentum and hydrophilicity of the biosilica film, the liquid continues to spread throughout the porous thin film after the initial pressure surge. Then, the meniscus retracts to establish the equilibrium state. It typically takes less than a minute for the system to reach steady state. The meniscus contacting the diatom is constantly monitored at the onset of the experiment. Extended flow duration experiments are important, because transient impacts that are not readily observable in shorter time frames may become apparent at larger intervals. For example, if the liquid spreads from the film to the microscope slide or the film dries before the reservoir empties, the micropump may initially appear to reach steady state, but is actually operating incorrectly. Based on the stable meniscus shape, constantly wetted film and the fact that liquid did not spread beyond the film to the microscope slide, it was concluded that the negative pressure provided by the porous biosilica film was driving flow continuously from the reservoir into the film. A flow duration of 48 h was noted before the next system check confirmed that the reservoir had completely emptied.

As mentioned in Sect. 2.4, flow rate in our microfluidic system was measured by capturing the meniscus position inside the reservoir over the course of experiments, as shown in Fig. 11. This allows us to obtain flow rates over the course of an experiment by finding the linear displacement of the meniscus between two consecutive photos, converting the linear displacement to volumetric displacement, using the time stamp embedded in the images to determine time lapse, and finally finding flow rate by dividing volumetric displacement by the time lapse. For the 25 mm^2 biosilica film with degassed DI water, the flow rates determined over the course of the experiment at different heating temperature are plotted in Fig. 12. It is clear that the flow rate maintains a relatively constant value for a wide range of temperatures. All diatom films used in our experiments produce graphs similar to

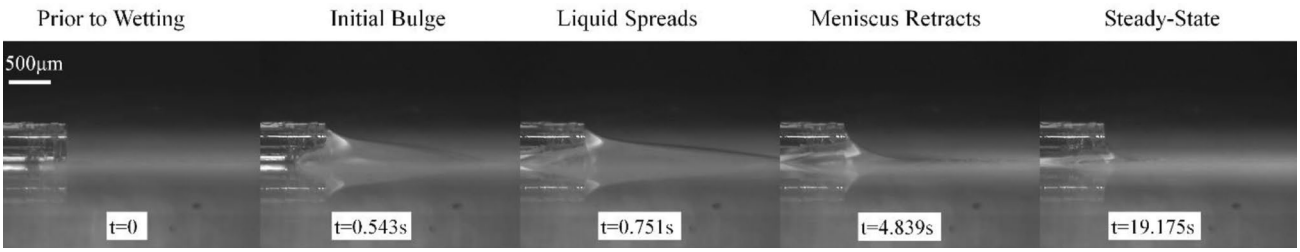

Fig. 10 Evolution of the meniscus outside the capillary tube until the steady state

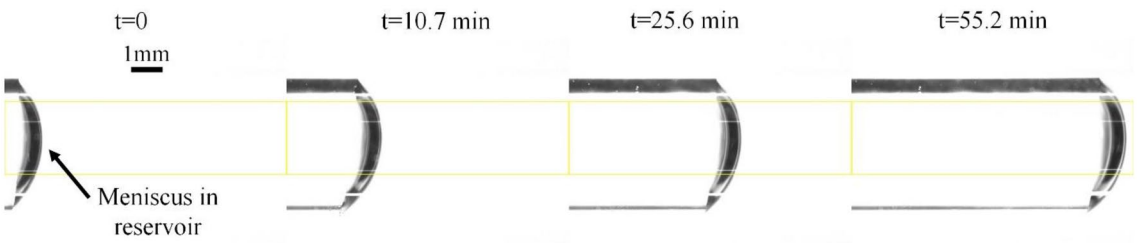

Fig. 11 Snapshots of meniscus receding in the reservoir during the operation of 25 mm^2 diatom film at 25 °C

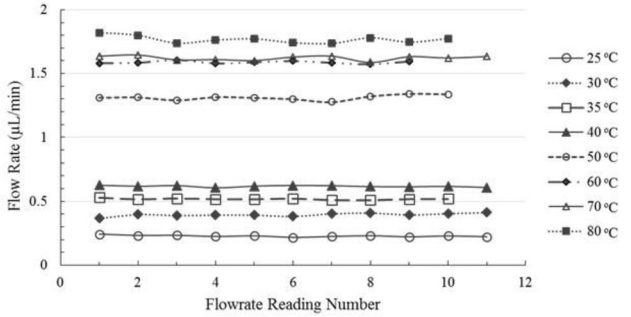

Fig. 12 Steady-state flow patterns of measured flow rates for 25 mm^2 diatom film at different temperatures

Fig. 12 and demonstrate the ability to pump steady amounts of liquid until the reservoir empties without cessation of flow. Relatively large or small gaps can occur between different temperature readings for a given film area, as demonstrated by the 40 °C and 50 °C data sets in Fig. 12, due to relatively large humidity fluctuations in the lab (the relative humidity varied between 35% and 50% in our experiments).

4.2 Flow rate analysis

To understand the effect of the diatom film area on flow, we plot the flow rate vs. the film area for untreated DI water at different substrate temperatures in Fig. 13a. The heating temperature varies from 25 to 60 °C. Flows tended to be similar for 64 mm^2 and 81 mm^2 films, which could be due to the disparity in film homgeneity for larger film sizes, as indicated in Fig. 3c. Minimum and maximum flow rates of 0.12 μL/min and 7.42 μL/min were achieved at 25 °C on a 9 mm^2 substrate and at 60 °C on an 81 mm^2 substrate, respectively. For a given temperature, as the film area increases, the flow rate increases due to larger evaporative area, as indicated in Eq. 1. It is clear from Fig. 13a that the line of flow rate vs. film area has a larger slope for higher temperature. For example, when the film area varies from 9 to 81 mm^2, the flow rate at 25 °C increases by 7.3 times (i.e., 0.12 μL/min → 0.88 μL/min), whereas the flow rate at 60 °C increases by 8.6 times (i.e., 0.862 μL/min → 7.42 μL/min). Thus, the effect of the evaporation area on the flow rate becomes stronger for a higher heating temperature. The experimentally determined flow rate from the open end of the reservoir when the capillary was not contacting the biosilica film, with the mensicus in the reservoir starting at the 0.7 mL mark that all flow rate experiments were conducted at, was 0.004 μL/min, which is much lower than the measured flow rate induced by the evaporation from the diatom biosilica film and, hence, was neglected in our study. To better understand the temperature effect on the flow rate, we replot the results according to the flow rate and temperature for different biosilica film geometries in Fig. 13b. The dependence of the flow rate on temperature is nearly linear. It is clear that the temperature effect on the flow rate becomes higher for the biosilica film of larger size. For the temperature varying from 25 to 60 °C, the flow rate increases by 7.1 and 8.4 times for 9 mm^2 and 81 mm^2 diatom film, respectively.

When using the untreated DI water, we noticed that bubbles started to form at the capillary tip at temperatures above 40 °C, causing fluctuations of meniscus location on the biosilica surface and occasionally cessation of flow. More discussion and analysis on this phenomenon can be found in Sect. 4.3. At temperatures above 60 °C, the flow rate data become very unstable due to the presence of the vapor bubbles. To minimize the possibility of bubble formation at high temperatures, we degassed the DI water via boiling. Then, experiments were repeated using the degassed DI water with

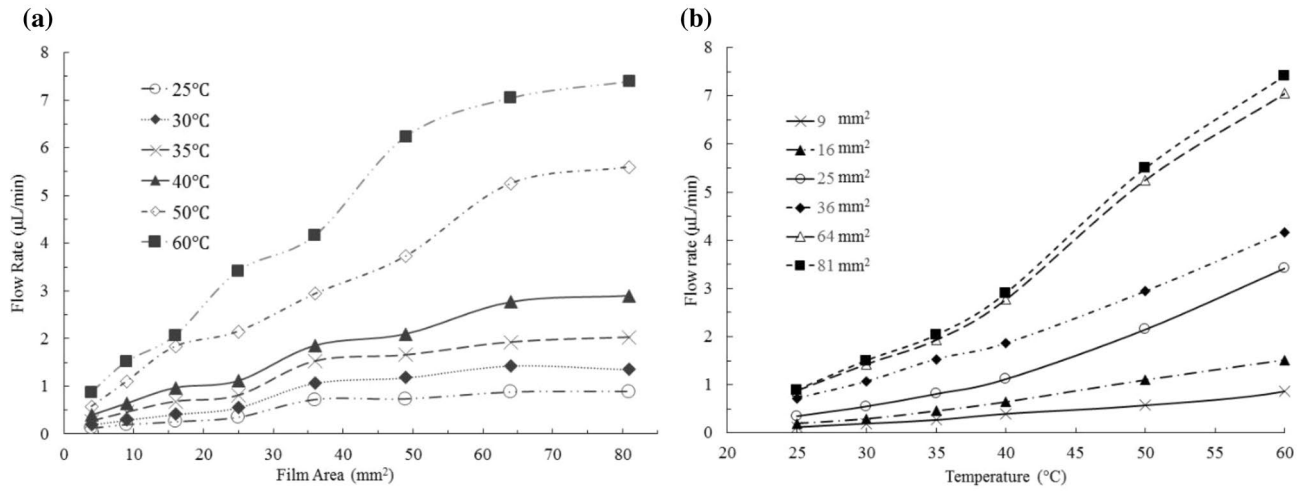

Fig. 13 Effects of diatom biosilica film area and heating temperature on the flow rate using untreated DI water: **a** the flow rate vs. the film area at different heating temperatures and **b** the flow rate vs. temperature

substrate temperatures ranging from 25 to 90 °C without bubble formation or cessation of flow. Figure 14 shows the impacts of diatom film area and heating temperature on the flow using degassed DI water, which is similar to Fig. 13. Using degassed DI water, minimum and maximum flow rates of 0.11 μL/min and 10.46 μL/min were achieved at 25 °C on a 9 mm^2 substrate and at 90 °C on an 81 mm^2 substrate, respectively. Similar to the results found in untreated DI water, increasing substrate area effectively increases flow rate at a given temperature, and the largest increase in flow rate occurs when the substrate temperature increases. Thus, higher temperatures provide a more efficient way of increasing flow rate for SERS applications.

The laminar boundary-layer model discussed in Sect. 3.3 is used to predict the flow rates for all substrate temperatures and areas in our experiments. The comparison of the flow rate between experiments and theoretic predictions is plotted in Fig. 15. There is good agreement between experimental measurements and theoretic predictions, especially in the relatively low-temperature range (i.e., < 50 °C). Therefore, it is reasonable to estimate the evaporation rate from the thin biosilica film by approximating it as a thin liquid film and using a modified laminar boundary-layer model, where the characteristic length is halved to compensate for the joining boundary layers from each edge. As the temperature rises, the prediction becomes less accurate and overestimates the flow rate. The possible reason is that experimental results were obtained in ambient conditions that ranged from ~ 23 to 24 °C and humidity values ranging from 35 to 50%, while a constant ambient temperature of 23 °C and humidity of 40% was used in the predictions.

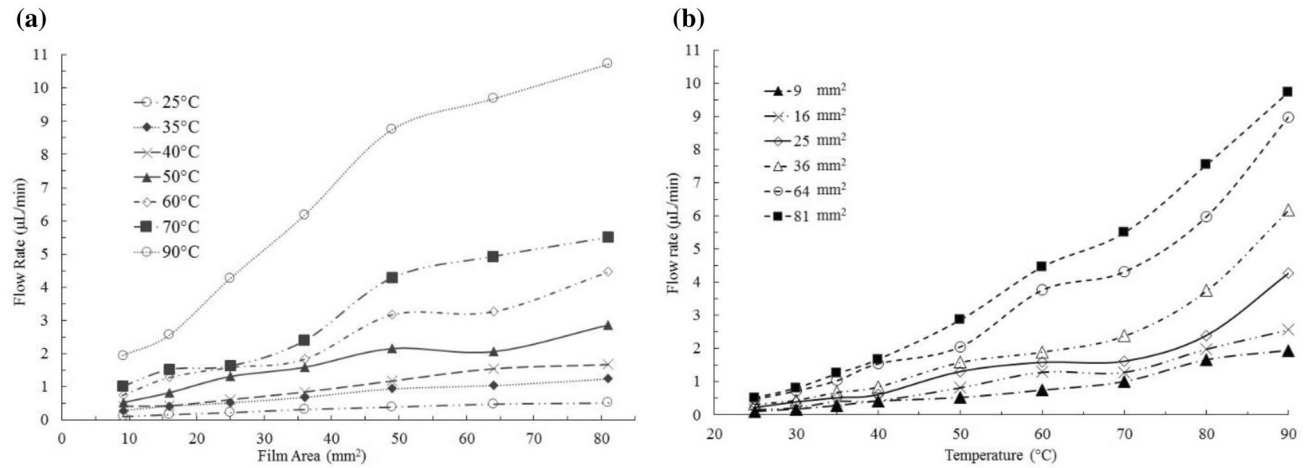

Fig. 14 Effects of biosilica film area and heating temperature on the flow rate using degassed DI water: **a** the flow rate vs. the film area at different heating temperatures; **b** the flow rate vs. temperature

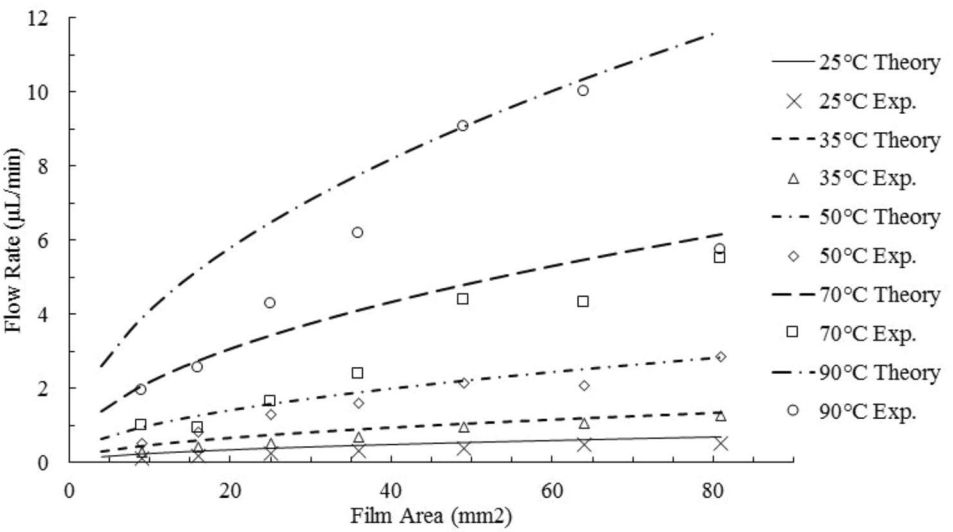

Fig. 15 Comparison of experimentally measured flow rate against theoretic predictions for different film areas and heating temperature

Originally, it was believed that evaporation through the nano-pores located on the diatom frustule, shown in Fig. 4b, would drive evaporation. However, theoretical results that attempted to use pore analysis, either using the nano-pores on an individual diatom or attempting to quantify the equivalent pore spacing between diatoms, demonstrated poor experimental correlation and were abandoned for the analysis provided in Sect. 3.3, which estimates flow due to evaporation by approximating the porous structure as a liquid film. The poor correlation is likely due to fact that the pore spacing and size were determined by approximating the diatoms as solid particles when, in fact, they are hollow. Another potential issue faced when approximating evaporation based on a circular pore is that, as seen in Fig. 4a, the pores created by the diatom frustules are irregularly shaped and difficult to quantify. However, the assumption of a solid particle in conjunction with the model used to determine capillary pressure induced by a porous medium is valid when attempting to determine capillary pressure, because it is a conservative estimate used to establish a system limitation. It is known that the hollow biosilica will have a smaller equivalent radius, R_c than a film comprised of solid particles, made with the same material, and with the same porosity. This smaller equivalent radius of the hollow film leads to a larger capillary pressure and flow rate. By approximating the hollow frustules as solid particles, it is known that the maximum flow rate determined using the capillary pressure model has a built-in factor of safety and that the system should always be capable of maintaining the calculated maximum flow rate. It should also be noted that the maximum experimental flow rates approached, but did not exceed the maximum predicted flow rate of 15.3 µL/min for films at 90 °C.

4.3 Flow stability

A stability analysis of the flow was performed to discover the root cause behind the cessation of flow at elevated temperatures for untreated DI water. In each experiment, high-contrast images of the meniscus outside the capillary tube and above the biosilica substrate, similar to the Fig. 9b, were obtained repeatedly over time periods ranging from 30 to 60 min on a 49 mm^2 substrate held at a set temperature. The edge of the liquid meniscus was found in each captured picture using our in-house developed MATLAB image processing code. The edges of the meniscus for a given experiment were plotted over each other to determine if the meniscus position fluctuated. The number of images over a given experiment ranged from 16 to 28 and the plots are provided for substrate temperatures varying from 23 to 70 °C in Fig. 16.

It can be clearly seen from Fig. 16a that when temperature varies from 23 to 35 °C, the meniscus curves captured at different times appear to remain constant. However, once the substrate temperatures increased to or beyond 40 °C, the meniscus location fluctuates signifying an instability. It was determined that the root cause of the instability was the bubble formation in the capillary tube, as shown in Fig. 17. The bubble would form, grow, and eventually burst at the capillary tip. The process of a growing bubble was repeated indefinitely until flow ceased. We think that the bubble formation was caused by the dissolved gasses in the DI water. As the liquid temperature increases, the equilibrium of dissolved gases in the liquid is broken, which results in the release of gases from liquid and hence the bubble formation. Thus, DI water degassed by boiling was used and confirmation experiments were run with a substrate temperature of 90 °C for 2 h, which had not been possible with untreated

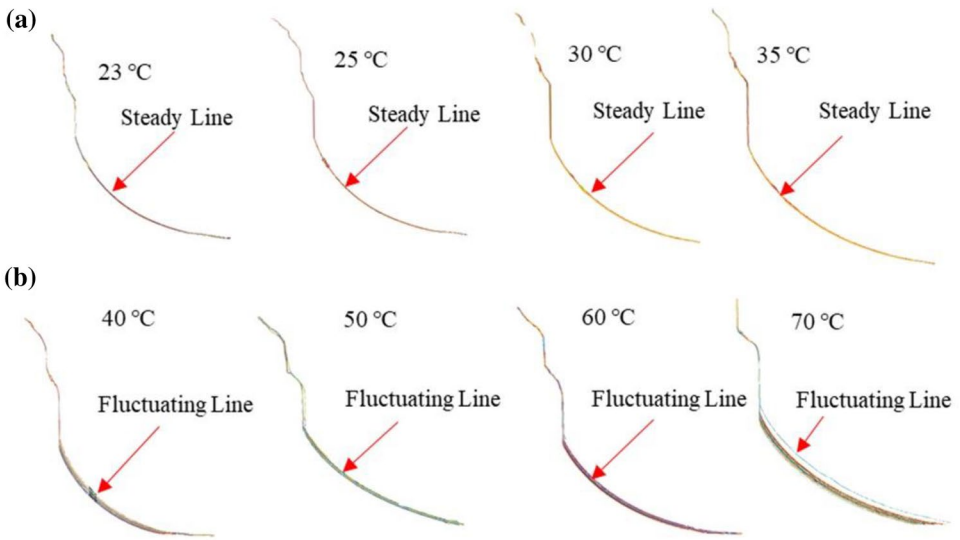

Fig. 16 Superposition of meniscus edges processed from experimental images during the operation time from 30 to 60 min: **a** stable meniscus at temperatures ranging from 23 to 35 °C; **b** unstable meniscus at temperatures ranging from 40 to 70 °C

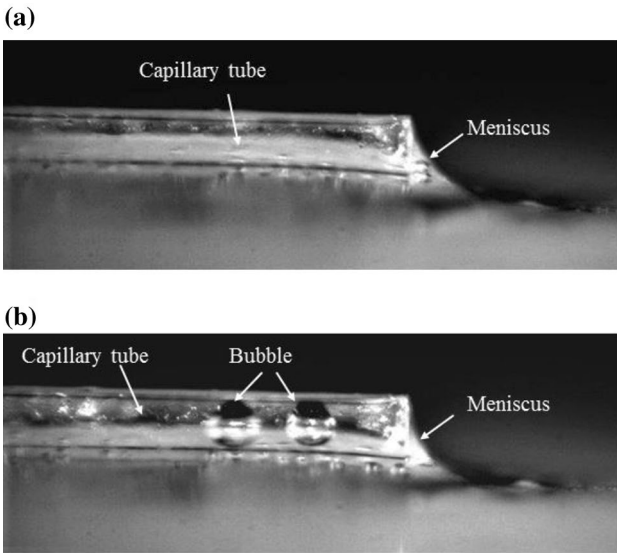

Fig. 17 Difference between a meniscus without a bubble formation and with a bubble formation: **a** no bubble and **b** bubble formed inside the capillary tube

DI water. With degassed DI water, steady-state patterns were achieved for all diatom films for high-temperature range.

5 Conclusion

In this study, a self-powered microfluidic pump using a porous, super-hydrophilic diatom biosilica thin film was proposed to transport fluid using a combination of capillarity and evaporation. Diatom biosilica thin films were fabricated using a drop-cast method. The microfluidic pump was created by joining a long, narrow reservoir filled with liquid to a capillary tube and contacting the capillary's tip to a porous film made of randomly oriented diatom biosilica frustules. To study the pumping capability of the proposed device, an experimental apparatus consisting of a 3D linear axis platform and high-resolution camera was designed and manufactured, which also controlled the temperature of the substrate through a logic-based feedback loop. A modified laminar boundary-layer model was applied to predict the evaporation rate and hence the flow rate. As the liquid flowed from the reservoir to the biosilica film, the meniscus in the pipette translated towards the capillary tip and was repeatedly imaged, which allowed the measurement of the flow rate through linear displacement.

We demonstrated the capability of diatom biosilica thin films to produce steady and continuous flow over 48 h due to their hydrophilic nature and that the flow rate can be controlled by manipulating the biosilica film area and heating temperature. We found that at higher substrate temperatures (i.e., > 40 °C), DI water needs to be degassed to maintain system stability and prevent flow cessation. The stability analysis of the flow revealed that the root cause of cessation was the bubble formation in the capillary tube from dissolved gases in the DI water at elevated temperatures. In our experiments, flow rates generated by our microfluidic pump varied between 0.109 and 10.46 μL/min for degassed DI water on films ranging from 9 to 81 mm^2 and at substrate temperatures varying between 25 and 90 °C. It was found that temperature had the greatest impact on flow rate for the tested range of substrate areas. The evaporation rates predicted from the boundary-layer model were in good agreement with the experimental measurements, signifying that the model can be used for design of evaporation-driven microfluidic devices.

Future work will focus on the fabrication of a microfluidic device using micro-manufacturing techniques to create a pump that can integrate μ-PIV flow measurement techniques to ascertain flow rate and particle distribution from the reservoir. The micropump device will be incorporated into an SERS system, where the detection limits and applicability will be determined.

Acknowledgements We are grateful to the National Science Foundation (NSF) for funding our research through CBET awards 1701339 and 1701329.

References

Bergman TL, Incropera FP (2011) Fundamentals of heat and mass transfer. 7th ed./Theodore 1. Bergman [and others], 7th edn. Wiley, Hoboken

Boyd-Moss M, Baratchi S, Di Venere M, Khoshmanesh K (2016) Self-contained microfluidic systems: a review. Lab Chip 16:3177–3192. https://doi.org/10.1039/C6LC00712K

Chen K-Y, Chen K-E, Wang K (2012) A flexible evaporation micropump with precision flow rate control for micro-fluidic systems. In: IEEE

Choi YH, Chung KH, Lee SS (2009) Microfluidic actuation by dehydration of hydrogel. In: IEEE

Convery N, Gadegaard N (2019) 30 years of microfluidics. Micro Nano Eng 2:76–91. https://doi.org/10.1016/j.mne.2019.01.003

Dollet B, Boulogne F (2017) Natural convection above circular disks of evaporating liquids. Phys Rev Fluids 2:053501. https://doi.org/10.1103/PhysRevFluids.2.053501

Effenhauser C, Harttig H, Krämer P (2002) An evaporation-based disposable micropump concept for continuous monitoring applications. Biomed Microdevice 4:27–32

Ever Aguirre L, Ouyang L, Elfwing A, Hedblom M, Wulff A, Inganäs O (2018) Diatom frustules protect DNA from ultraviolet light. Sci Rep 8:1–6

Goedecke N, Eijkel J, Manz A (2002) Evaporation driven pumping for chromatography application. Lab Chip 2:219–223. https://doi.org/10.1039/B208031C

Gordon R, Losic D, Tiffany MA, Nagy SS, Sterrenburg FAS (2009) The Glass Menagerie: diatoms for novel applications in nanotechnology. Trends Biotechnol 27:116–127. https://doi.org/10.1016/j.tibtech.2008.11.003

Guan Y-X, Xu Z-R, Dai J, Fang Z-L (2006) The use of a micropump based on capillary and evaporation effects in a microfluidic flow injection chemiluminescence system. Talanta 68:1384–1389

Jeffryes C, Campbell J, Li H, Jiao J, Rorrer G (2011) The potential of diatom nanobiotechnology for applications in solar cells, batteries, and electroluminescent devices. Energy Environ Sci 4:3930–3941. https://doi.org/10.1039/C0EE00306A

Jingmin L, Chong L, Zheng X, Kaiping Z, Xue K, Liding W (2012) A microfluidic pump/valve inspired by xylem embolism and transpiration in plants (a bio-inspired microfluidic pump/valve). Plos One 7:e50320. https://doi.org/10.1371/journal.pone.0050320

Juncker D et al (2002) Autonomous microfluidic capillary system. Anal Chem 74:6139–6144

Kearns H, Bedics MA, Shand NC, Faulds K, Detty MR, Graham D (2016) Sensitive SERS nanotags for use with 1550 nm (retina-safe) laser excitation. Analyst 141:5062–5065

Kim H, Kim K, Lee SJ (2016) Compact and thermosensitive nature-inspired micropump. Sci Rep 6:36085

Kirby BJ (2010) Micro- and nanoscale fluid mechanics: transport in microfluidic devices. Cambridge University Press, New York

Kitahama Y, Ozaki Y (2016) Surface-enhanced resonance Raman scattering of hemoproteins and those in complicated biological systems. Analyst 141:5020–5036

Kong X et al (2016) Optofluidic sensing from inkjet-printed droplets: the enormous enhancement by evaporation-induced spontaneous flow on photonic crystal biosilica. Nanoscale 8:17285–17294

Kong X et al (2017) Detecting explosive molecules from nanoliter solution: a new paradigm of SERS sensing on hydrophilic photonic crystal biosilica. Biosens Bioelectron 88:63–70

Kraai JA, Rorrer GL, Wang AX (2019) Highly-porous diatom biosilica stationary phase for thin-layer chromatography. J Chromatogr A 1591:162–170

Laser DJ (2004) Areview of micropumps. J Micromech Microeng 14:R35–R64

Li Y-J, Yang Y-N, Zhang H-J, Xue C-D, Zeng D-P, Cao T, Qin K-R (2019) A microfluidic micropipette aspiration device to study single-cell mechanics inspired by the principle of wheatstone bridge. Micromachines. https://doi.org/10.3390/mi10020131

Lin S, Lin S, Zhu W, Jin Y, Crozier KB (2013) Surface-enhanced Raman scattering with Ag nanoparticles optically trapped by a photonic crystal cavity. Nano Lett 13:559–563

Long DA (2002) The Raman effect: a unified treatment of the theory of Raman scattering by molecules. Chichester Press, Chichester

Lynn NS, Dandy DS (2009) Passive microfluidic pumping using coupled capillary/evaporation effects. Lab Chip 9:3422–3429. https://doi.org/10.1039/B912213C

Marshall KE, Robinson EW, Hengel SM, Pasa-Tolic L, Roesijadi G (2012) FRET imaging of diatoms expressing a biosilica-localized ribose sensor. PLoS One 7(3):e33771

Masoodi R, Pillai KM, Masoodi R, Pillai KM (2012) Wicking in porous materials: traditional and modern modeling approaches. CRC, Boca Raton

Namasivayam V (2003) Transpiration-based micropump for delivering continuous ultra-low flow rates. J Micromech Microeng 13:261–271

Nie C, Frijns AJH, Mandamparambil R, Toonder JMJ (2015) A microfluidic device based on an evaporation-driven micropump. (Report), p 17

Ohno KI, Tachikawa K, Manz A (2008) Microfluidics: applications for analytical purposes in chemistry and biochemistry. Electrophoresis 29:4443–4453

Otto A (1992) Surface-enhanced raman scattering. J Phys Condens Matter 4:1143–1212

Ren F, Campbell J, Hasan D, Wang X, Rorrer GL, Wang AX (2013) Surface-enhanced Raman scattering on diatom biosilica photonic crystals. 8598:85980N-85980N-85988

Sackmann EK, Fulton AL, Beebe DJ (2014) The present and future role of microfluidics in biomedical research. Nature 507:181. https://doi.org/10.1038/nature13118

SE-FIT (2018) https://www.se-fit.com/about/

Sivashanmugan K, Squire K, Kraai JA, Tan A, Zhao Y, Rorrer GL, Wang AX (2019) Biological photonic crystal-enhanced plasmonic mesocapsules: approaching single-molecule optofluidic-SERS sensing. Adv Opt Mater 7:1900415

Squires TM, Quake SR (2005) Microfluidics: fluid physics at the nanoliter scale. Rev Mod Phys 77:977–1026

Taylor J, Huefner A, Li L, Wingfield J, Mahajan S (2016) Nanoparticles and intracellular applications of surface-enhanced Raman spectroscopy. Analyst 141:5037–5055

Temiz Y, Skorucak J, Delamarche E (2014) Capillary-driven microfluidic chips with evaporation-induced flow control and dielectrophoretic microbead trapping vol 8976. In: SPIE

Turner APF (2013) Biosensors: sense and sensibility. Chem Soc Rev 42:3184–3196. https://doi.org/10.1039/C3CS35528D

Wang J, Ahmad H, Ma C, Shi Q, Vermesh O, Vermesh U, Heath J (2010) A self-powered, one-step chip for rapid, quantitative and multiplexed detection of proteins from pinpricks of whole blood. Lab Chip 10:3157–3162. https://doi.org/10.1039/c0lc00132e

White FM (1991) Viscous fluid flow. McGraw-Hill, New York

Woias P (2005) Micropumps—past, progress and future prospects. Sens Actuators B Chem 105:28–38

Xiao-Ming C et al (2019) A capillary-evaporation micropump for real-time sweat rate monitoring with an electrochemical sensor. Micromachines 10:457. https://doi.org/10.3390/mi10070457

Xu Z-R, Zhong C-H, Guan Y-X, Chen X-W, Wang J-H, Fang Z-L (2008) A microfluidic flow injection system for DNA assay with fluids driven by an on-chip integrated pump based on capillary and evaporation effects. Lab Chip 8:1658–1663. https://doi.org/10.1039/B805774E

Xu Y-h, Yan W-p, Qin K-r, Cao T (2019) Three-dimensional flow field simulation of steady flow in the serrated diffusers and nozzles of valveless micro-pumps. J Hydrodyn 31:413–420. https://doi.org/10.1007/s42241-018-0121-7

Zhang A, Zha Y, Zhang J (2014) A surface acoustic wave micropump to pump fluids from a droplet into a closed microchannel using evaporation and capillary effects. AIP Adv 4:127144

Zhou Q, Kim T (2016) Review of microfluidic approaches for surface-enhanced Raman scattering. Sens Actuators B Chem 227:504–514

Zimmermann M, Bentley S, Schmid H, Hunziker P, Delamarche E (2005) Continuous flow in open microfluidics using controlled evaporation. Lab Chip 5:1355–1359

Zimmermann M, Schmid H, Hunziker P, Delamarche E (2007) Capillary pumps for autonomous capillary systems. Lab Chip 7:119–125. https://doi.org/10.1039/B609813D